The Nonlinear Turbulent Dynamo

Jason Maron[1] and Steve Cowley[2]

UCLA

ABSTRACT

We simulate the evolution of an initially weak magnetic field in forced turbulence for a range of Prandtl numbers. The field grows exponentially with the Kulsrud-Anderson $k^{3/2}$ spectrum until the magnetic energy approaches the viscous-scale kinetic energy, where the magnetic forces then backreact on the velocity. Further growth proceeds more slowly until a saturated state is reached where the magnetic and kinetic energies are equal, and where the magnetic energy exists primarily at the resistive scale. We discuss the structure of this turbulence and the extrapolation of the results to astrophysically-large Prandtl numbers.

1. Introduction

Microgauss magnetic fields are observed in spiral galaxies and between galaxies in clusters [Zweibel & Heiles (1997), Kronberg (1994), Vallee (1998), Beck et. al. (1996)]. In cluster plasmas the fields have coherence lengths of up to $10kpc$ (Taylor et. al., 1999). In galaxies the magnetic fields are ordered over the whole galaxy and have energy densities comparable to the turbulent energy density. It is not known if the fields originated before during or after galaxy formation. Most current research centers around dynamo theories where turbulent motions amplify the field from an initial weak seed field to its present strength and structure [Ruzmaikin et. al. (1988), Kulsrud (1999), Zweibel & Heiles (1997), Beck et. al. (1996)] Indeed some kind of dynamo seems to be the most plausible explanation of the observations. However, despite considerable progress over forty years the dynamo theory is not complete and thus the history of galactic and extra galactic fields is uncertain. The galactic dynamo (if it exists) differs from the more familiar solar dynamo [Mestel, Weiss] and geodynamo [Glatzmaier & Roberts 1995] in two key ways. First the disc geometry of the galaxy clearly affects the magnetic field dynamics. Secondly the ratio of viscosity to resistivity, the magnetic Prandtl number (P_r), is of order 10^{15} in the warm partially ionized interstellar medium but only $1 - 10^{-2}$ in the solar convection zone. We shall also discuss here the possibility of dynamos in fully ionized plamas such as protogalaxies and early galaxies. In this paper we show that high Prandtl number dynamos are profoundly different from low Prandtl number dynamos.

[1]maron@tapir.caltech.edu

[2]steve.cowley@ic.ac.uk

The galactic spatial scales and their associated timescales suggest a *possible* scenario for field growth. Elements of this scenario are suggested by the work of Kulsrud and Anderson (1992) and, particularly for Stage 3, Field, Blackman and Chou (1999). We take this scenario as a framework for discussion and not as proven. Indeed our calculations already expose flaws in the scenario. First consider the important space and time scales from the largest to the smallest. The galaxy itself is about 10^{10} years old, $10 - 15kpc(= \lambda_g)$ across and rotates with velocity $\sim 200km/s$ once every 2×10^8 years. Supernovae produce random velocities of order $10km/s$ on a scale $100pc(= \lambda_f)$ and with timescales of order 10^7 years. Approximately $5 - 15\%$ of the kinetic energy at the supernova scale is helical [Moffatt 1978]. Without a magnetic field the kinetic energy cascades to small viscous scales, λ_ν, where $\lambda_\nu \sim 0.1 - 0.01pc$. The viscous eddies turnover on a timescale $\tau_\nu \sim 10^5$ years. Finally the smallest scale is the resistive scale, λ_η which is typically 10^3km – truly negligibly small. We will assume that the initial field is very weak. Such fields can be made in many different ways, see for instance Gnedin & Ferrara, & Zweibel (2000) who find that fields of order 10^{-18} Gauss can be made in shocks during the re-ionization phase of structure formation. We divide the growth into three stages.

Stage 1. The Kinematic Small Scale Field Dynamo. During this stage the field is too weak to affect the velocity at any scale. Since the eddies at the viscous scale turnover the fastest they amplify the field first. Therefore the growth time is approximately 10^5 years in our galaxy. This growth was first predicted by Batchelor (1950), and later Kazantsev (1968), who also investigated the structure of the field, and still more recently Kulsrud and Anderson gave a spectral theory of the process (1992). In the 1990s the kinematic theory was considerably refined [Schekochihin, et. al. (2001), Chertkov et. al. (1999)] and it is well understood. Much of what is understood comes from the short correlation time kinematic model in which the velocity correlation time is assumed infinitesimal. The important features of the magnetic field evolution in this model are: first, the magnetic spectrum $E_b(k,t)$ rises as $k^{3/2}$ at all k much less than the peak, k_p. Second, for $k < k_p$, $E_b(k,t)$ grows as $\exp(3/4\gamma t)$ at fixed k with γ roughly the turnover rate of the viscous scale eddies. The peak wavenumber, k_p increases as $k_p \propto \exp(3/5\gamma t)$ until it reaches, and remains at, the resistive scale ($k_\eta \sim 1/(\lambda_\eta) \sim \sqrt{\gamma/\eta}$ with η the resistivity). Finally the magnetic field is in a folded state [Schekochihin et. al., 2001], where the variation of $\mathbf{B}$ along itself ($< |\mathbf{B} \cdot \nabla \mathbf{B}|^2 >$) is much smaller than the variation of B across itself ($< |\mathbf{B} \times (\nabla \times \mathbf{B})|^2 >$). All these features of the kinematic phase evolution are seen, at least qualitatively, in the early stages of our simulations. Clearly the field predicted by the small scale field dynamo is on scales much smaller than the observed galactic field. Therefore Stage 1 is necessarily a transitory stage. When the magnetic field energy becomes of order the energy in the viscous scale eddies the kinematic stage (Stage 1) ends. In the galaxy this corresponds to a magnetic field strength of $0.1\mu G$.

Stage 2. Approach to Equipartition. While magnetic forces at the end of Stage 1 can change the viscous scale flows they are not strong enough to affect the more energetic larger scale motions. The strain of these larger scale motions continues to amplify the field. One would expect that they act on the field in a way similar to the viscous scale eddies in Stage 1, but on a slower

timescale. As the field grows more of the velocity spectrum is affected by the magnetic forces (see Section 5.). Eventually on a timescale of a few large eddy turnover times the magnetic energy becomes of order the kinetic energy of the large stirring scale motions. In the galaxy the timescale for this is the supernova stirring time – roughly 10^7 years. On this timescale the galactic rotation and the helical component of the turbulence have negligible effect.

This stage is porrly understood and it is the main subject of this paper. In 1981 Meneguzzi and Poquet computed the turbulent amplification of magnetic fields in a $P_r \sim 1$ plasma. They showed that without helicity the magnetic energy grew until it saturated at about 15% of the kinetic energy. The magnetic and kinetic spectra resemble our higher resolution, $P_r \sim 1$, computations (for example see Fig. 3). There is no evidence from these simulations (or our own) that there is energy equipartition scale by scale. In the $P_r \gg 1$ case, the majority of the magnetic energy is in the scales between the viscous and (smaller) resistive scale. Almost none of the kinetic energy is contained in these sub-viscous scales.

Recently there has been considerable interest in simulating Alfven wave turbulence [Maron & Goldreich (2001), Cho & Vishniac (2000), Biskamp & Muller (2000)]. Identical magnetic and kinetic power law spectra ($k^{-\alpha}$ with $\alpha = 1.5 - 1.6$) are seen. These simulations start with magnetic energy on the large scale that is stronger or of order the kinetic energy of the forcing scale. Dynamo simulations must, of course, start with small fields. It is not clear that the final state is independant of the initial conditions – at least for times less than the resistive time of the large scales.

At the end of Stage 2. the magnetic energy is expected to be of order the kinetic energy of the forcing motions. The observed field is on scales bigger than the supernova forcing scale. There is no evidence from our simulations that there is any large scale field at the end of Stage 2 – indeed the majority of the magnetic energy is in the subviscous scales.

Stage 3. Large Scale Field Growth.

The final stage of the magnetic field evolution is growth of the field on the largest scale, the galactic scale. It is believed [Poquet et. al. (1977), Meneguzzi & Poquet (1981), Field et. al. (1999), Brandenburg (2000)] that the helicity of the turbulence plays a key role in this *inverse cascade*. Indeed Field, Blackman and Chou (1999) have argued that this stage is very similar to the kinematic ($\alpha - \omega$) mean field dynamo [Parker (1979), Moffatt (1978), Ruzmaikin (1988)]. The estimated timescale for the mean field dynamo in the galaxy is 2×10^8 years [Field et. al., (1999), Kulsrud (1999)]. This timescale is controlled by the slow rotation of the galaxy that gives ω and drives the helicity in the turbulence to give α. The fraction of the turbulent energy in the galaxy that is helical is about $5 - 15\%$?? Recent simulations by Maron and Blackman (2001) suggest that large scale field growth at such low helical fractions is not possible (although it is at 100% helicity [Brandenburg (2000)]. They also show that the fractional helicity needed to see large scale field growth increases with magnetic Prandtl number. There is an ongoing debate about the effect of small scale fields on the mean field dynamo – several authors have claimed a quenching (suppression) of the alpha effect [Hughes & Cattaneo (1996), Gruzinov et. al. (1996), Bhattachargee (1996)].

Blackman and Field (2000) have pointed out the important role of boundary conditions that allow the magnetic helicity of one sign to be discarded. Without such boundary conditions they claim that mean field growth is on a negligably slow resistive time [Gilbert]. The field we obtain at the end of stage 2 is highly striped (i.e. it reverses in sign on a small resistive scale). Since the mean field dynamo motions will amplify both the positive and negative stripes one would expect amplification of the small scale field to dominate. However we will not consider this stage in any detail in this paper. It is clear that this stage is dependant on the geometry and physical conditions in the galaxy and therefore simulations in simplified homogeneous models may be missleading.

There are four key results from our simulations. First, the energy of the magnetic field grows to a saturated level equal to the kinetic energy of the stirred flow. Second, the magnetic field energy is contained in the small resistive scales. Third, the field is in the form of long thin folds (stripes) where the variation of $\mathbf{B}$ across itself is much faster than the variation of $\mathbf{B}$ along itself. Fourth, the predominant straining and folding of the field in saturation comes from the stirring scale motions.

2. Equations

We investigate MHD turbulence in situations of interest to the origin of the galactic magnetic field. Various regimes exist depending on the state of the dynamical medium, specifically on whether it is charged or neutral. In an ionized plasma, if the magnetic field is sufficiently strong, charged particle transport is confined to magnetic fieldlines and the kinematic diffusivity has the anisotropic Braginskii form (section 2.1). If neutrals are present, viscosity is isotropic. If additionally the magnetic energy density is sufficiently high, ambipolar diffusion can arise from the differential ion-neutral motion. Magnetic diffusivity in all cases is due to resistivity. We also consider the artificial but illustrative problem involving ordinary viscosity and resistivity (section 4). We consider these regimes in the context of the galaxy and protogalaxy, where kinematic diffusivities greatly exceed magnetic diffusivities.

The equations of magnetohydrodynamics (MHD) are

$$\rho\left(\partial_t \mathbf{v} + \mathbf{v}\cdot\boldsymbol{\nabla}\mathbf{v}\right) = -\boldsymbol{\nabla}\left(P + \frac{\mathbf{B}^2}{8\pi}\right) - \boldsymbol{\nabla}\cdot\Pi + \frac{1}{4\pi}\mathbf{B}\cdot\boldsymbol{\nabla}\mathbf{B} + \rho\nu\nabla^2\mathbf{v} \tag{1}$$

$$\partial_t \mathbf{B} = \boldsymbol{\nabla}\times(\mathbf{v}\times\mathbf{B}) + \eta\nabla^2\mathbf{B} \tag{2}$$

$$\partial_t \rho + \boldsymbol{\nabla}\cdot(\rho\mathbf{v}) = 0, \tag{3}$$

$$\partial_t c + \boldsymbol{\nabla}\cdot(c\mathbf{v}) = \nu_c\nabla^2 c \tag{4}$$

$$\boldsymbol{\nabla}\cdot\mathbf{B} = 0 \tag{5}$$

$$\Pi = -3\nu_{ii}(\hat{B}\hat{B} - \frac{1}{3}I)(\hat{B}\hat{B} - \frac{1}{3}I) : \boldsymbol{\nabla}\mathbf{v} \tag{6}$$

$\mathbf{v}$	fluid velocity	$\mathbf{B}$	magnetic field
ρ	fluid density	P	fluid pressure
ν	momentum diffusivity	η	magnetic diffusivity
c	passive scalar density	ν_c	passive scalar diffusivity
Π	Braginskii pressure	$\hat{B}$	Magnetic unit vector

Table 2: Dynamical variables

Π is the Braginskii tensor, which applies when charged particle transport is confined to fieldlines. Ambipolar diffusion can optionally be added if the fluid is only partially ionized, and if magnetic forces are strong enough to generate significant differential ion-neutral velocities.

We simplify equations 1-4 for applications in this paper. The magnetic field is measured in velocity units with $\mathbf{b} \equiv \mathbf{B}/\sqrt{4\pi}$. Incompressibility is assumed throughout, so we set $\rho = 1$. We these modifications, equations 1-4 transform to

$$\partial_t \mathbf{v} = -\mathbf{v} \cdot \boldsymbol{\nabla}\mathbf{v} - \boldsymbol{\nabla}(P + \frac{\mathbf{b}^2}{2}) - \boldsymbol{\nabla} \cdot \Pi + \mathbf{b} \cdot \boldsymbol{\nabla}\mathbf{b} + \nu\nabla^2\mathbf{v}, \tag{7}$$

$$\partial_t \mathbf{b} = \boldsymbol{\nabla} \times (\mathbf{v} \times \mathbf{b}) + \eta\nabla^2\mathbf{b}, \tag{8}$$

$$\boldsymbol{\nabla} \cdot \mathbf{v} = 0, \qquad \boldsymbol{\nabla} \cdot \mathbf{b} = 0. \tag{9}$$

$$\partial_t c + \mathbf{v} \cdot \boldsymbol{\nabla} c = \nu_c \nabla^2 c. \tag{10}$$

Incompressibility is implemented by first calculating $\partial_t \mathbf{v}$ without the fluid and magnetic pressure terms, and then by projecting the resulting Fourier components transverse to $\mathbf{k}$. This procedure accounts for the divergence introduced by the Braginskii term.

2.1. Tensor viscosity

Particle transport in a fully ionized medium is confined to fieldlines if the collision length exceeds the cyclotron radius:

$$B \gtrsim \frac{c\, m_p^{1/2} n_p e^3}{k^{3/2}} T^{-3/2} \sim 2.7 \cdot 10^{-6} n_p T^{3/2}$$

This condition is easily satisfied except possibly in the early protogalaxy where the field may have been very weak. For ionized plasmas, we use the Braginskii pressure (Eq. 6) in place of the Laplacian viscosity.

3. Simulation

3.1. Scales

We state our assumptions for the parameters of galactic turbulence in table 4, followed by a discussion of our inability to directly simulate them.

Table 4: Galactic turbulence parameters

Quantity	Symbol	Galactic	Protogalactic
Magnetic coherence scale	λ_g	10^{22} cm	-
Forcing scale	λ_f	10^{21} cm	10^{23} cm
Forcing velocity	v_f	10^6 cm/s	10^7 cm/s
Viscous scale	λ_ν	10^{17} cm	10^{22} cm
Resistive scale	λ_η	10^{12} cm	10^{12} cm
Viscosity	ν	10^{20} cm$^2/s$	10^{29} cm$^2/s$
Magnetic diffusivity	η	10^{14} cm$^2/s$	10^{10} cm$^2/s$
Prandtl number	P	10^6	10^{19}
Neutral free path	λ_{nn}	10^{15} cm	-
Ion free path	λ_{ii}	10^{13} cm	10^{22} cm
Temperature	T	10^4 K	10^7 K
Proton density	n	1cm^{-3}	10^{-2}cm^{-3}

The range of scales involved in the galactic dynamo poses the chief obstacle to simulation. A spectral grid of 256^3 elements delivers a scale range of ~ 50, which is enough to capture self-similar dynamics or to study transitions between regimes occuring at different scales. The phases of the dynamo can be simulated separately and then spliced together to construct a complete picture. Limitations exist of course, most notably when we consider the growth of a large scale field in the presence of a tangled small scale field. In the galactic setting, these scales differ by orders of magnitude.

In the high-Prandtl linear regime, the dominant magnetic structure exists between the viscous and the resistive scales. We find that at least an order of magnitude of separation between them is necessary to capture the $k^{3/2}$ Kulsrud-Anderson spectrum. In our simulations, a Prandtl number of at least 2500 is required.

Our principal concern regarding the nonlinear stage is the final state of the magnetic field in the limit of large inertial range and Prandtl number, and how long it takes to get there. Specifically, is this field dominated by large or small scale structure, or equivalently how does the spectral index compare to -1? Finally, does the result for larger Prandtl number differ from that for $P = 1$?

In the nonlinear stage, the magnetic field is strong enough to backreact on the turbulence. This first occurs at the viscous scale, then at successively larger scales in the inertial range as the

magnetic field grows. The objective is to study the backreaction on the inertial-range structure when the magnetic energy is at the resistive scale. It is important that the forcing occur at a substantially larger scale than the viscosity so that it doesn't interfere with the magnetic backreaction. Thus we require $\lambda_\eta << \lambda_\nu << \lambda_f$. In a 256^3 spectral simulation, the effective scale range is ~ 50, and so we can have a factor of ~ 7 separating each scale. To study the role of viscosity and the inertial range, we ran 5 simulations with λ_ν engineered to have a sequence of values from λ_η to λ_f.

3.2. Computational scales

Table 5 defines the scales that occur in the simulation of the turbulent dynamo. When the Prandtl number is greater than or equal to unity, the scales have the ordering $\lambda_f > \lambda_\nu \geq \lambda_\eta$. The dynamics occur between λ_f and λ_a, and so we set $\lambda_f \sim 1$ and $\lambda_\eta \sim \lambda_a$, where the simulation volume is a cube of side length 1 and λ_a is the smallest resolved scale. We ran a sequence of simulations with λ_ν varying between λ_f and λ_a. A forcing power of unity at the outer scale maintains an RMS outer scale velocity of $v_f \sim 1$.

Table 5: Computational scales

v_λ	Velocity at scale λ	b_λ	Magnetic field at scale λ
ν	Kinematic diffusivity	η	Resistive diffusivity
λ_ν	Viscous scale	λ_η	Resistive scale
λ_f	Forcing scale (= 1)	$\mathbf{v}_f$	Outer scale RMS velocity (=1)
λ_s	Shear scale	v_s	Shear velocity
$\lambda_a = 3/N$	Aliasing (resolution) scale	N^3	Grid size
$t_f \sim \lambda_f/v_f$	Forcing timescale	$t_s \sim \lambda_s/v_s$	Shear timescale
$\lambda_\perp$	Transverse folding scale	$\lambda_\parallel$	Longitudinal folding scale
$f = \lambda_\parallel/\lambda_\perp$	Fieldline folding factor	$s = k/(2\pi) = 1/\lambda$	Wavenumber

During the weak magnetic field regime, the following scalings enable us to set λ_ν and λ_η by varying ν and η. Below the forcing scale and above the viscous scale, the velocity has the form of a Kolmogorov cascade with $v_\lambda \sim v_f(\lambda/\lambda_f)^{1/3}$. The eddy time is $t \sim \lambda/v_\lambda$. The viscous scale arises from equating the eddy time with the viscous time.

$$\lambda_\nu \sim (\nu\lambda_f^{1/3}/v_f)^{3/4} \tag{11}$$

Below the viscous scale, the velocity has the form of a uniform shear with the same timescale as the eddy time at the viscous scale: $t_\nu \sim \lambda_f^{1/2}\nu^{1/2}v_f^{-3/2}$. Equating this with the resistive time, $t_\eta \sim \lambda_\eta^2/\eta$, we obtain the resistive scale $\lambda_\eta \sim \eta^{1/2}\lambda_f^{1/4}\nu^{1/4}v_f^{-3/4}$. We engineer η so that λ_η is equal

to the grid scale $\lambda_a \sim \lambda_f/N$, where N is the number of grid elements on each cube edge. This establishes a condition on η as a function of ν:

$$\eta_g \sim \frac{\lambda_f^{3/2} v_f^{3/2}}{\nu^{1/2} N^2} \tag{12}$$

Equating the viscous and resistive times, the Prandtl number is related to the ratio of scales as

$$\frac{\lambda_\nu}{\lambda_\eta} \sim \frac{\nu^{1/2}}{\eta^{1/2}} \sim P_r^{1/2} \tag{13}$$

In designing a simulation with a specified Prandtl number greater than or equal to unity, one uses the above scalings to select ν and η. For studies of the kinematic backreaction, it is desirable to have λ_ν small enough so that a true kinematic inertial range exists, say $\lambda_\nu \sim \lambda_f/8$.

Once the magnetic field is strong enough to backreact on the velocity, the shear scale is set by the eddies which have the same energy density as the magnetic field. In the saturated state, the magnetic energy grows to the forcing energy, and the shear time increases to the forcing time. Simultaneously, the resistive scale increases by a factor of $(\lambda_f/\lambda_\nu)^{1/3}$ from its value in the linear regime.

3.3. Code

We withhold for now all details about the code not necessary for understanding the results, which we put off until section B. The equations of MHD are solved spectrally and incompressibly, and with periodic boundaries. A standard 256^3 grid with spatial dimension 1^3 has Fourier wavenumbers $s = k/(2\pi)$ extending from -85 to +85, where we have employed the 2/3 aliasing truncation. Wavenumbers and physical scales are related by $\lambda k = \lambda 2\pi s = 2\pi$. Viscosity and resistivity are of the k^2 type ($\nu\nabla^2 v$ and $\eta\nabla^2 b$) unless the Braginskii viscosity is invoked. Finally, define the one-dimensional kinetic and magnetic energy spectra as

$$E_v = \int E_v(s) ds \qquad\qquad E_b = \int E_b(s) ds. \tag{14}$$

The parameters for each simulation are given in table 7.

3.4. Uniform field and helicity

The simulations in this work have zero mean magnetic field and are forced with zero mean kinetic helicity. Fractional fluctuations in the kinetic helicity exist at the level of 10 percent. The magnetic helicity is initially zero and subsequently fluctuates about zero at an amplitude of 5 percent of the maximum potential magnetic helicity.

Our simulations have no mean magnetic field or helicity, to establish what large-scale can be created in their absence. This is the nonlinear kinematic dynamo problem. If indeed the final state is dominated by small-scale magnetic energy, then the necessity of other mechanisms such as helicity or Keplerian shear may be invoked for the next stage of the dynamo.

3.5. Folded fieldline structure

The magnetic field, in the course of amplification and entanglement, develops structure not identifiable in the power spectrum. Define

$$k_\perp^2 =< (\mathbf{b} \times \nabla \times \mathbf{b})^2 > / < b^4 > \qquad k_\parallel^2 =< (\mathbf{b} \cdot \nabla \mathbf{b})^2 > / < b^4 > \tag{15}$$

$$k_P^2 =< \left(\nabla \frac{b^2}{2} \right)^2 > / < b^4 > \qquad k_\circ^2 =< (\mathbf{b} \cdot \nabla \times \mathbf{b})^2 > / < b^4 > \tag{16}$$

Define a fieldline folding factor $f = k_\perp / k_\parallel$, which parameterizes the magnetic tension per energy and the unwinding time of fieldlines. Also define a measure of the magnetic scale based on the power spectrum:

$$k_b^2 = \int k^2 E_b(k) dk / \int E_b(k) dk \tag{17}$$

We normalize with $< b^4 >$ instead of $< b^2 >^2$ because it has the same kurtosis statistics as the squared magnetic force terms. In the simulations, $k_\perp / k_b \sim 0.58$ with fluctuations of 3 percent, whereas the kurtosis varies by 200 percent (Schekochihin, et. al., 2001). Therefore, either $k_\perp$ or k_b may be used to define the magnetic scale.

3.6. Timescales

We identify timescales for resistivity (t_η), vorticity (t_w), and shear (t_s) by defining:

$$t_\eta = \frac{1}{k_\perp^2 \eta} \qquad t_w = 2\pi < (\nabla \times v)^2 >^{-1/2} \qquad t_s =< b^2 > \tag{18}$$

t_η reflects a balance between shear and resistivity. t_w corresponds to the eddy shear time and the magnetic growth rate during the linear regime. t_s is indirectly linked to the shear time through $t_s \sim b^2 \sim v_s^2 \sim \lambda_s / v_s$, where b is the saturation magnetic field, and λ_s and v_s correspond to the scale and velocity of the dominant shear.

3.7. Viscous scale

We define the viscous scale λ_ν to correspond to the peak of the function $k^3 E_v(k)$ during the linear regime, which reflects the dominant scale of the shear.

3.8. Spandex waves

MHD interactions exist which are non-local in k space. For instance, large-scale shear can transfer energy directly to small-scale magnetic fields. Alfvén waves are an oscillatory phenomenon where small-scale perturbations interact with a uniform magnetic field. A similar oscillatory phenomenon exists in a tangled magnetic field. Here, a large-scale velocity perturbation generates a backreaction in a small-scale tangled field. Locally, magnetic forces act in all directions, but spatially averaged, they tend to act collectively to oppose the original large-scale perturbation.

Define a Lagrangian displacement field $\zeta = \hat{\mathbf{a}} e^{i(\mathbf{k}\cdot\mathbf{x}-\omega t)}$, with $\mathbf{k}\cdot\hat{\mathbf{a}} = 0$ and $\mathbf{v} = d_t\zeta$. Let $\mathbf{b} = \mathbf{b}_0 + \hat{\mathbf{a}}(\mathbf{b}_0\cdot\mathbf{k}) i e^{i(\mathbf{k}\cdot\mathbf{x}-\omega t)}$, where $\mathbf{b}_0$ is the static non-oscillatory part with an assumed scale of much less than k^{-1}. Any other time evolution in $\mathbf{v}$ and $\mathbf{b}$ is neglected, as well as viscosity and resistivity. $\mathbf{b}$ satisfies the induction equation $\mathbf{b} = \int d_t\mathbf{b}\, dt = \mathbf{b}\cdot\nabla\zeta$. Returing to the Navier Stokes equation, $< d_t\mathbf{v} >= -\omega^2 e^{i(\mathbf{k}\cdot\mathbf{x}-\omega t)} =< \mathbf{b}\cdot\nabla\mathbf{b} >=< \mathbf{b}_0\cdot\nabla\mathbf{b}_0 > - < (\mathbf{b}_0\cdot\mathbf{k})^2 > e^{i(\mathbf{k}\cdot x-\omega t)}$. An average is taken over scale k, which implies $< \mathbf{b}_0\cdot\nabla\mathbf{b}_0 > \sim 0$ and $< (\mathbf{b}_0\cdot\mathbf{k})^2 > \sim < (\mathbf{b}_0)^2 > k^2/3$. ζ has an oscillatory eigenmode with phase speed $< (\mathbf{b}_0)^2/3 >^{1/2}$. This is equivalent to the Alfvén speed if we only consider the averaged magnetic field component along $\mathbf{k}$.

4. Exponential growth of a weak magnetic field

The magnetic field is initially weak during the linear stage, and the kinetic spectrum has the Kolmogorov form. Magnetic fields grow exponentially at the rate of the turbulent shear. Since the viscous-scale eddies shear the fastest, magnetic growth proceeds at the viscous timescale t_ν.

The resistive scale of the magnetic field is determined by a balance between shear growth and resistive decay: $t_s \sim \lambda_\eta^2/\eta$. We identify the resistive scale λ_η with the transverse scale $\lambda_\perp$ (equation 15). From the beginning to the end of the nonlinear stage, $\lambda_\perp$ increases by a factor of $(\lambda_f/\lambda_\nu)^{1/3}$, as is observed in table 6.

4.1. Kulsrud-Anderson theory for the linear regime.

Kulsrud and Anderson (1992) (also Kazantsev 1968, Gruzinov, Cowley, Sudan 1996, Schekochihin, Boldyrev, Kulsrud 2001) found that a dynamically weak magnetic field grows exponentially with a $k^{3/2}$ spectrum terminating at the resistive scale. The magnetic spectrum evolves according

to

$$\partial_t E_b(k) = \frac{\gamma}{5}\left(k^2\partial_k^2 E_b(k) - 2\partial_k E_b(k) + 6E_b(k)\right) - 2\frac{k^2\eta}{4\pi}E_b(k) \tag{19}$$

which has the solution

$$E_b(k,t) \sim k^{3/2} K_0\left(\frac{5\eta}{2\pi\gamma}k\right) e^{(3/4)\gamma t} \tag{20}$$

where $\gamma \sim \int k E_v(k) dk$. $E_v(k)k^{3/2}$ is the shearing rate at scale k.

We ran simulations starting from a weak magnetic field for a sequence of 5 viscosities, all with Prandtl number ≥ 1. Their ID numbers are A1 through A5 (table 7), and their energy and spectral evolutions are shown in figures 1 and 2. Magnetic energies grow exponentially in all cases until the nonlinear stage is reached. The growth rates t_g are given in table 6, where they are expressed in the form $E_b(t) \sim e^{t/t_g}$. The $k^{3/2}$ exponent is seen only when $P_r \geq 2500$, as with simulation A1, where sufficient range exists between the viscous and resistive scales (figure 2). The $k^{3/2}$ spectrum is especially robust in the simulation with zero resistivity (simulation A0, figure 2). This simulation is not without concern for its physical validity, a matter which we address in sections 5.5 , 5.8 , and 5.7.

Table 6: Energies and timescales

Sim	ν	η	E_v linear	E_v sat	E_b sat	t_g linear	t_w linear	t_w sat	t_η linear	t_η sat	$s_\perp$ linear	$s_\perp$ sat
A1	$5{\cdot}10^{-2}$	$2{\cdot}10^{-5}$	0.2	.16	.17	1.41	1.5	1.55	4.38	8.8	17.0	12.0
A2	$5{\cdot}10^{-3}$	$1{\cdot}10^{-4}$	0.75	.38	.32	.59	.45	.62	1.50	3.5	13.0	8.5
A3	$3{\cdot}10^{-3}$	$1{\cdot}10^{-4}$	0.8	.40	.32	.46	.35	.47	1.26	3.5	14.2	8.5
A4	$1{\cdot}10^{-3}$	$1{\cdot}10^{-4}$	0.9	.60	.22	.36	.25	.30	.78	3.1	18.0	9.0
A5	$4{\cdot}10^{-4}$	$4{\cdot}10^{-4}$	1.5	.60	.16	.65	.12	.23	.30	1.8	14.6	6.0
B1	$5{\cdot}10^{-2}$	$1{\cdot}10^{-5}$	-	.16	.17	-	-	2.0	-	12.9	-	14.0
B2	$5{\cdot}10^{-3}$	$4{\cdot}10^{-5}$	-	.3	.4	-	-	.69	-	4.4	-	12.0
B3	$3{\cdot}10^{-3}$	$4{\cdot}10^{-5}$	-	.3	.3	-	-	.57	-	4.4	-	12.0
B4	$1{\cdot}10^{-3}$	$4{\cdot}10^{-5}$	-	.5	.3	-	-	.31	-	3.5	-	13.4
B5	$4{\cdot}10^{-4}$	$1{\cdot}10^{-4}$	-	.55	.3	-	-	.20	-	3.4	-	8.6
B6	$1{\cdot}10^{-4}$	$1{\cdot}10^{-4}$	-	.55	.3	-	-	.11	-	3.1	-	9.0

"Linear" and "sat" denote the linear and satuated states, averaged over a suitable length of time. E_v and E_b are the kinetic and magnetic energies. t_g is the exponential magnetic growth time during the linear phase. t_w is the vorticity time, t_η is the resistive time, and $s_\perp$ is the magnetic wavenumber.

The 256^3 simulations were run for half of a crossing time, long enough to establish the saturated spectra and $s_{\|}$, but not long enough to accurately determine E_v, E_b, and t_w.

The magnetic kurtosis, $< b^4 > / < b^2 >^2$, is observed to rise from ~ 3 to ~ 15 during the linear regime, and then to return to ~ 3 in the saturated state. These results are discussed in Schekochihin, Cowley, Maron, & Malyshkin (2001).

For each value of the viscosity, the resistivity is assigned the smallest value such that magnetic energy is destroyed by resistivity rather than dealiasing.

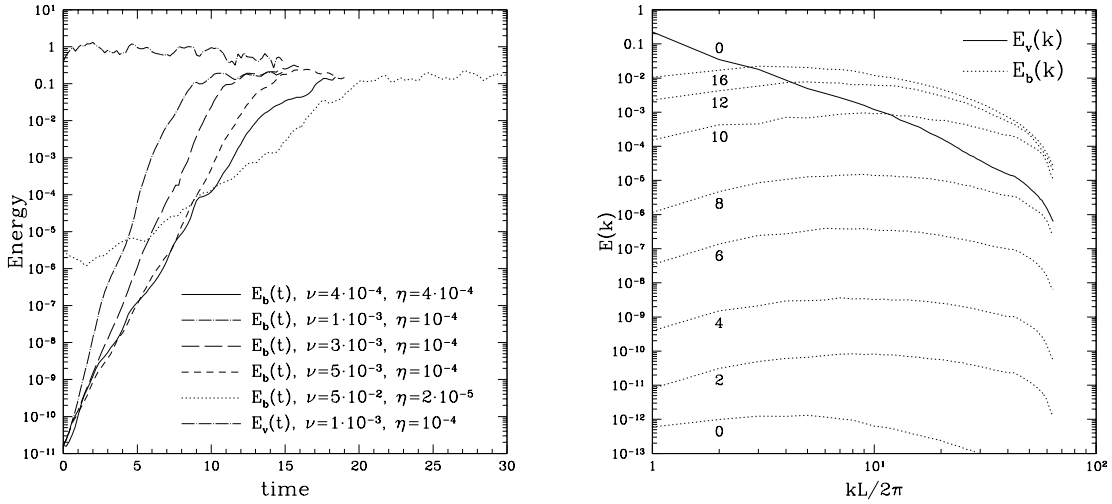

Figure 1. Left: The exponential magnetic energy growth for a sequence of viscosities. Parameters for the simulation (A1 through A5) are given in table 7. Right: The evolution of the magnetic spectrum for simulation A3. Numbers indicate times. The spectrum at the latest time is in the saturated state.

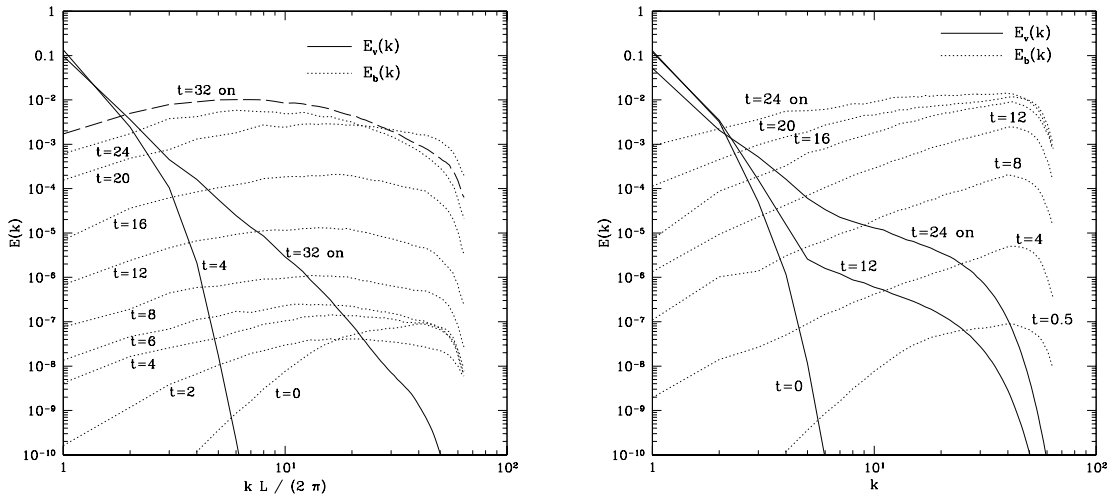

Figure 2. Left: The kinetic and magnetic energy spectra for simulation A1, $P_r = 2500$, $\nu = 5 \cdot 10^{-2}$, $\eta = 2 \cdot 10^{-5}$. Right: The same quantities for simulation A0, $\nu = 5 \cdot 10^{-2}$, $\eta = 0$. The Prandtl

number is undefined, however for this resolution and viscosity, any value above 10^4 *is functionally equivalent.*

5. Magnetic saturation

Saturation is the long-term asymptotic state of MHD turbulence in the absence of a mean magnetic field and with zero mean kinetic helicity. We postulate that the dynamics are characterized by four principles: 1) The kinetic and magnetic energies are approximately equal. 2) Magnetic energy forward cascades according to the forcing timescale. 3) Magnetic fieldline folding and tangling prevents the field from unwinding. 4) The magnetic field preferentially aligns with the neutral shear frame. These principles lead to a magnetic spectrum of the form k^{-1} that is independent of viscosity. The spectrum is terminated at a resistive scale that is set by a balance between forcing and resistivity: $\lambda_\eta \sim (t_f \eta)^{1/2}$.

The fastest kinematic shear is due to the viscous-scale eddies if the kinetic spectrum is more shallow than k^{-3}, otherwise it is due to the forcing-scale eddies. In the linear regime, where the kinetic spectrum has the form $k^{5/3}$, the viscous-scale eddies shear fastest. In this regime, shear functions to transfer energy from the velocity to the magnetic field, and so the magnetic field grows at the rate of the viscous-scale eddies.

In the nonlinear regime, the magnetic backreaction opposes shear that is less energetic than the magnetic field. This effect can be nonlocal in Fourier space, where small-scale magnetic fields can oppose large scale shear. In the saturated state, where the kinetic and magnetic energies are equal, only the forcing-scale eddies are energetic enough to shear the magnetic field. Shear exists on smaller time and energy scales, yet we argue that some fraction of it results from a transfer of magnetic energy to the velocity, rather than the other way around. Or, energy can be cyclically exchanged between $\mathbf{v}$ and $\mathbf{b}$, such as for spandex waves (section 3.8).

The magnetic field has a reduced tension per energy compared to what would be expected from random phase structure. The reduction is typically by a factor of 10 for a 128^3 simulation, as evaluated by the parameterization in section 3.5. Therefore, less generation of small scale velocities by the unwinding of small scale magnetic fields occurs. The reduction is great enough so that the magnetic energy cascades from the forcing scale to the resistive scale without significant loss to unwinding. This phenomenon is exhibited in the tension release simulations of section 5.4, and is reflected by the independence of the magnetic spectrum on viscosity.

In the simulations with an initially weak magnetic field, the magnetic spectrum is dominated by small scale energy at the beginning of the nonlinear stage, and in subsequent evolution it stays this way. One may ask if the result would be different if we started instead with a large scale, large energy field. Any small scale field that is formed should because the fieldline structure is not yet folded and the tension is strong. We observe instead that the magnetic struture evolves to a small-scale dominated state identical to the result of a weak initial field simulation. The likely

reason for this is that fieldlines tangle, and even if they are energetically able to unwind, topological constraints prevent them. In general, we have never observed magnetic hysteresis in any of the simulations.

Figure 3 illustrates the nonlinearly saturated spectra for a sequence of viscosities, all at fixed resistivity. The magnetic spectra all fall in the same place, with the exception of the one having the highest viscosity. This suggests that the kinematics at any scale other than the forcing scale are irrelevant to the cascade. The kinetic spectra also have greatly reduced magnitudes compared to the magnetic spectra at high k.

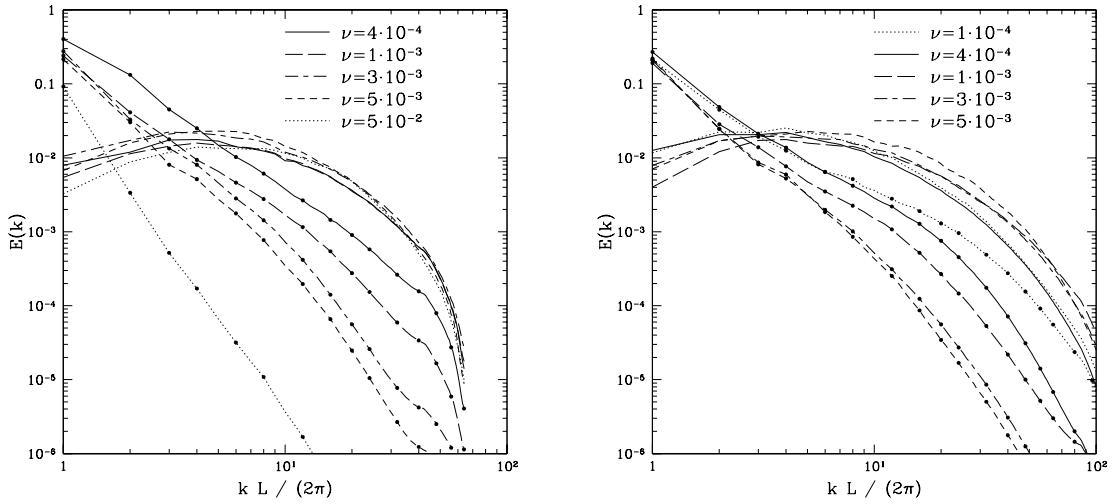

Figure 3: The saturated spectra for a sequence of viscosities and fixed resistivity. Lines with points indicate the kinetic spectra, and lines without points indicate the magnetic spectra. The simulations in the left and right panels have 128^3 *and* 256^3 *resolution, respectively. The ID numbers for the* 128^3 *simulations are A1 through A5, and for the* 256^3 *simulations they are B2 through B6.*

5.1. Magnetic growth during the nonlinear phase

During the linear stage, the magnetic energy is less than the viscous-scale energy ($b < v_\nu$), and the velocity spectrum has the Kolmogorov form. The fastest shear (t_s) is due to the viscous-scale eddies: $\lambda_s \sim \lambda_\nu$, $v_s \sim v_\nu$, and $t_s \sim t_\nu$. The nonlinear stage begins when $b \sim v_\nu$. Thereafter, growth slows as the shear velocity grows according to $v_s \sim b$. At and above the shear scale, the velocity still has the Kolmogorov form, and the shear time is $t_s \sim \lambda_s/v_s \sim \lambda_f v_s^2/v_f^3 \sim \lambda_f b^2/v_f^3$. Growth ends when $b \sim v_f$ and $t_s \sim t_f$.

The resistive scale of the magnetic field is determined by a balance between shear growth and resistive decay: $t_s \sim \lambda_\eta^2/\eta$. We define $\lambda_\eta = \lambda_\perp$ (equation 15). From the beginning to the end of the nonlinear stage, $\lambda_\perp$ increases by a factor of $(\lambda_f/\lambda_\nu)^{1/3}$. The data in table 6supports this scaling, although comparison is inexact because the forcing velocity, and hence the shear time,

change slightly from the linear to the saturated state.

The magnetic enegy grows during the nonlinear stage in our 3 dimensional simulations, whereas in the 2 dimensional simulations of Kinney et. al. 2000, it decays. In 2D, they found that an initially weak field grows exponentially at the resistive scale until nonlinearity occurs, after which the field decays.

5.2. Timescales and the neutralization of shear

According to the backreaction hypothesis, shear motions below the forcing scale have a dimished role in cascading the magnetic field. If true, then the vorticity time t_w reflects some shear motions not associated with the cascade of the magnetic field, whereas the resistive time t_η more accurately reflects the magnetic cascade time. We therefore expect a greater change in t_η from the linear to the saturated state than for t_w, and we also expect t_η to be more approximately constant as a function of viscosity than t_w. Both of these conclusions are well supported by the data in table 6. t_η is not expected to be exactly constant in the saturated state because the larger viscosities influence the forcing-scale velocities, and hence E_v and the shear rate.

5.3. Large initial magnetic field

Kulsrud-Anderson predict that an initially weak field grows exponentially with a $k^{3/2}$ spectrum, which simulation confirms. The $k^{3/2}$ spectrum is independent of the initial spectral shape. The magnetic energy is therefore dominated by small-scale structure at the beginning of the nonlinear phase, and remains so through subsequent evolution to the saturated state. One may ask if the result would be different if the magnetic field were initially strong and organized at low k. We will find that there is no hysteresis in the saturated state from the results in this section, and in section 5.7 on resolution refinement.

Simulation L3 has an initial magnetic energy of unity, which is confined to modes with $k/2\pi \leq 4$. The viscosity is $3 \cdot 10^{-3}$, and the resistivity is 10^{-4}, both of which are identical to simulation A3. The viscous scale is smaller than the initial magnetic scale. Subsequent evolution restores the magnetic spectrum to the saturated state of simulation A3, as show in figure 4.

A more stringent test is to initialize a strong large-scale magnetic field which has no topological linkage. Such a field can resist bending by the turbulence and possibly oppose the formation of small scale field. If the field is topologically linked, then even though tension forces exist, they may be unable to release the tension. The question is, do linkages form in a strong magnetic field?

The field of $b_2 = 2\sin(2\pi x_1)$ is a simple example having zero mean and an energy density of unity, and constitutes the initial conditions of simulation L4. The initial velocity is zero, and the forcing power is unity. The viscosity is 10^{-3} and the resistivity is 10^{-4}, which are identical to

simulation A4. The magnetic field evolves to the saturated state A4 after 5 time units.

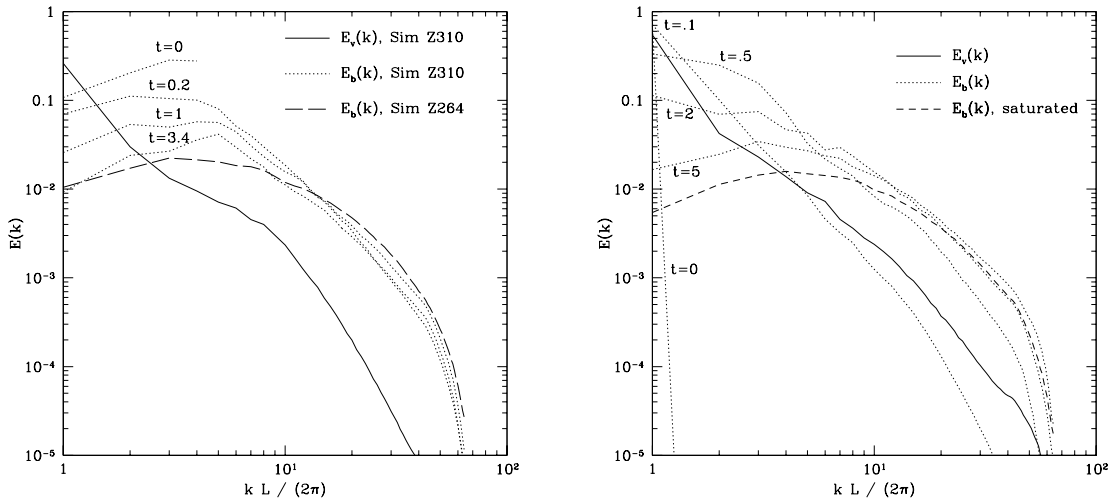

Figure 4. Left: this figure follows the evolution of an initially large magnetic field at low k (simulation L3), until it reaches a state where the magnetic energy is dominantly at high k. The dashed line is the time-averaged saturated state of simulation A3, which has the same viscosity and resistivity. Right: This figure follows simulation L4, which is similar to L3 except that the initial field is at even lower k. The dashed line is the time-averaged saturated state of simulation A4, which has the same viscosity and restivity.

5.4. Interaction between the velocity and the magnetic field

The reduced magnetic tension of the saturated state was previously diagnosed by noting that $\lambda_\parallel/\lambda_\perp >> 1$. A more direct test can be constructed by observing how fast magnetic tension generates kinetic energy. This is done by artificially setting the velocity to zero and observing the release of tension in the subsequent evolution. Specifically, we note how much new kinetic energy is generated from fieldline unwinding, and where in Fourier space it appears. Folded fieldlines have less tension per energy than structureless fieldlines, and hence unwind more slowly, generating less velocity. The random-phase magnetic field defined in appendix C serves as a reference for structureless fieldlines. A random-phase field is generated from a structured field by randomizing the Fourier component orientations while preserving the power spectrum. The structured magnetic field generates more velocity than the random-phase field, verifying that it has reduced tension per energy (figure 5).

We draw from the nonlinearly saturated state of simulation A4 at $t = 12$ to initialize two test simulations. In simulation U4, we erased the velocity and restarted with the same viscosity. The resistivity was reduced to 10^{-5} to remove the effect of resistive magnetic energy loss. In simulation U4r we additionally randomize the phases of the magnetic Fourier modes. A random phase magnetic field has a folding factor of unity, and serves as a reference for assessing structure.

By comparing the kinetic spectra generated in simulations U4 and U4r, we can evaluate the degree of folding present in U4.

We also observe that small scale magnetic fields generates large scale velocities, while the random-phase field generates small scale velocities. Specifically, the original magnetic field at $s \sim 15$ generates velocities at $s \sim 3$, while the random phase field generates them at $s \sim 15$. We infer that for the dynamics of the saturated state, only large scale shear is responsible for the magnetic cascade, even though the kinetic spectrum is more shallow than k^{-3}. Therefore, the cascade proceeds according to one timescale, the forcing timescale. This also supports our claim that magnetic forces oppose shear that is less energetic than the magnetic field. Finally, the absence of production of kinetic energy beyond $s = 6$ establishes that unwinding of the small scale field is unimportant. The magnetic energy cascades from the forcing scale to the viscous scale without loss to the velocity.

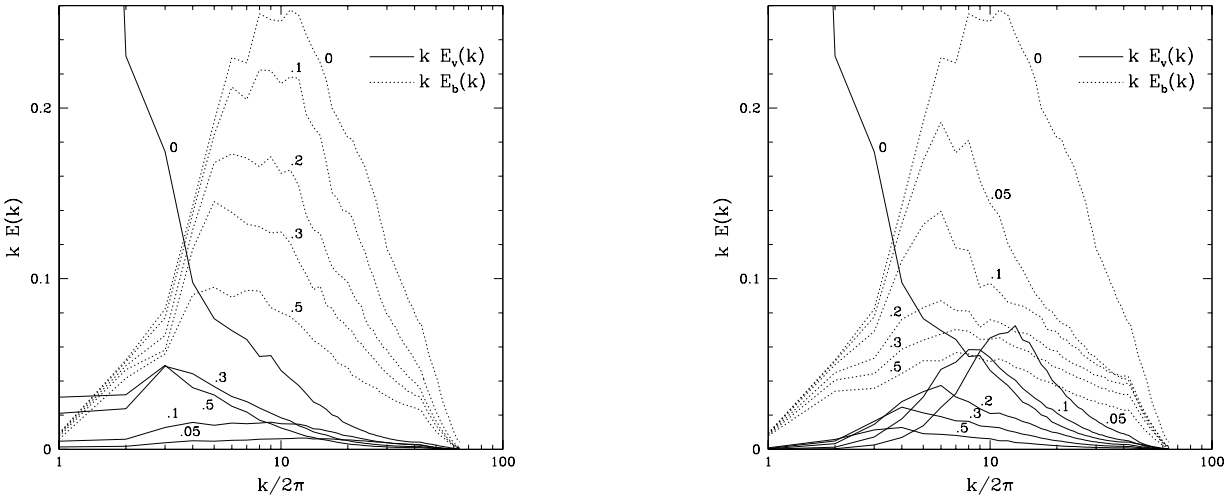

Figure 5. Left: Simulation U4. Right: Simulation U4r. Numbers indicate times. These simulations are discussed in section 5.4. At $t = 0$, we show the kinetic spectra from before the velocity was artificially set to zero.

5.5. Folding scales

We evaluated the longitudinal and transverse folding scales $\lambda_\parallel$ and $\lambda_\perp$ of the saturated states for a range ν and η (figure 6). For a 128^3 simulation, and for η larger than 10^{-4}, we find that $\lambda_\perp \sim \lambda_\eta \sim \eta^{1/2}$, which would be expected if the shear timescale is constant and shear balances resistivity. $\lambda_\parallel$ is approximately constant and equal to the outer scale of unity. For $\eta < 10^{-4}$, decreasing the resistivity does not further decrease $\lambda_\perp$, but it does decrease in $\lambda_\parallel$ and the folding factor. This occurs because for these low values of η, dealiasing of the magnetic field disrupts folded structure (section 5.7). We interpret the lowest attainable value of $\lambda_\perp$ as the resolution limit.

For a 256^3 simulation, the resolution limit is reached at $\eta \sim 4 \cdot 10^{-5}$. At this resolution, $\lambda_\perp$ is smaller than for a 128^3 simulation, while $\lambda_\parallel$ is unchanged. Further reduction of η does not further reduce $\lambda_\perp$.

The saturated spectra for varying resistivity at fixed viscosity are generated by a process of resaturation, whereby we take a saturated state, change the resistivity, and continue evolution until the system has reached a new equilibrium state. This process is described in section 5.7. The initial conditions are always taken from one of the simulations in the series A1 through A5. 256^3 simulations are initialized by doubling the grid of the appropriate 128^3 simulation, resetting the resistivity, and then evolving to the new saturated state.

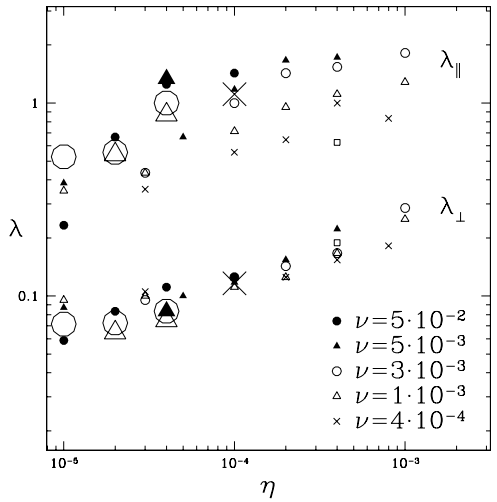

Figure 6: The upper and lower rows of points correspond to the longitudinal and transverse folding scales defined in section 3.5. These numbers come from the saturated states of simulations for a range of values in ν and η. Small symbols represent 128^3 simulations, and large symbols represent 256^3 simulations. The square points in the figure represent a 64^3 simulation with a Braginskii viscosity of $\nu_T = .003$, and with $\eta = .0004$. This establishes that fieldline structure is folded in this simulation.

5.6. Unwinding

For scales large enough to be uninfluenced by viscosity, magnetic fieldlines release tension in one Alfvén time: $t_A \sim \lambda_\parallel / b$. Below the viscous scale, the viscous and the magnetic tension terms dominate in the Navier Stokes equation: $\nu v_u / \lambda_\perp^2 \sim b^2 / \lambda_\parallel$, where v_u is the velocity at which magnetic structures zunwind. The viscous unwinding time is then $t_u \sim \lambda_\parallel / v_u \sim \lambda_\parallel^2 \nu / (\lambda_\perp^2 b^2)$. We have accounted for the possibility of folded magnetic structure by distinguishing between $\lambda_\perp$ and $\lambda_\parallel$.

Magnetic energy is lost Alfvénically if $t_A > t_u$, otherwise it is lost viscously or resistively,

whichever is faster. The transition between Alfvén and viscous unwinding occurs at a scale λ_A such that $t_A \sim t_u$. Assume a spectrum of $E_b(k) \sim k^{-1}$, or $b \sim \lambda^0$. We consider two limiting cases for the folding structure. If $\lambda_\parallel \sim \lambda_f$, then $\lambda_A \sim \lambda_f^{1/3}\lambda_\nu^{2/3}$. If $\lambda_\parallel \sim \lambda_\perp$, then $\lambda_A \sim \lambda_\nu^{4/3}\lambda_{\mathbf{f}}^{-1/3}$.

At small scales, where viscosity mediates unwinding, we ask which is faster, shear or unwinding. If $t_s < t_u$, then the magnetic energy cascades without loss to the resistive scale, which is determined by a balance between shear and resistivity: $\lambda_\eta \sim (t_s\eta)^{1/2}$. The magnetic energy would then grow to be equal to the forcing energy. If $t_s > t_u$, then the magnetic energy must adjust itself to restore $t_s \sim t_u \sim t_\eta$. We define the resistive scale to be equal to the transverse magnetic scale: $\lambda_\eta = \lambda_\perp$.

The ratio of the unwinding to the shear time is

$$\frac{t_u}{t_s} \sim \frac{\lambda_\parallel^2}{\lambda_s^2}\frac{v_s^2}{b^2}\frac{\nu}{\eta} \tag{21}$$

Simulation suggests that the magnetic field and the shear eddies have the same energy: $b^2 \sim v_s^2$, and that the folding scale is such that $\lambda_\parallel \sim \lambda_f$. We assume that the Kolmogorov scaling applies above the shear scale: $v_s^3\lambda_f \sim v_f^3\lambda_s$.

If $t_u > t_s$, then $b \sim v_f$ and $\lambda_s = \lambda_f$, and consistency with (21) requires that

$$\Lambda \equiv \frac{\nu}{\eta}\frac{\lambda_\parallel^2}{\lambda_f^2} \geq 1. \tag{22}$$

If $\Lambda < 1$, then unwinding balances shear, and b^2 decreases to bring about $t_u \sim t_s \sim t_\eta$. The shear time and the magnetic scale both contract until $\lambda_\eta \sim (\eta t_f)^{1/2}\,\Lambda^{1/6}$. The magnetic energy is then $b^2 \sim v_f^2\Lambda^{1/3}$.

5.7. Resolution refinement

We found in section 5.3 that the saturated state is free from hysteresis. There, we compared the final state of simulation A4, which started from weak magnetic field conditions at high k, with that of simulation L4, which started from strong magnetic field conditions at low k. The viscosity and resistivity are the same in each of these simulations. In this section, we consider the effect of changing the resistivity.

In a process which we call resaturation, we take the saturated state from a finished simulation, change the resistivity, and then continue the simulation until a new saturated state is reached. Simulations A4s and A5s were thus obtained from simulations A4 and A5, respectively. In simulations A4s and A5s, the resistivity was reduced to 10^{-6}.

Simulations A4w and A5w have the same ν and η as A4s and A5s, but they were started instead from a weak initial magnetic field with an energy of 10^{-6}. The saturated spectra for A4s and A4w are identical, as are the ones for A5s and A5w.

The new saturated states for simulations A4s and A5s were reached in a time equal to one third of the forcing time. Whereas the technique of resaturation has now been validated, we can thus obtain the saturated states for any combination of ν and η with little computational effort. This procedure was exploited to obtain the data used in section 5.5, and also to obtain the saturated spectra of the 256^3 simulations B1 through B6.

Simulation A4s develops only slightly more small-scale magnetic field than simulation A4. This is because the resistivity is small enough so that the spectral aliasing procedure contributes to magnetic energy loss, which destroys folded fieldline structure and increases the magnetic tension per energy. We show this with the tension spectrum in figure 7. The extra magnetic forces generate velocities which dissipate viscously, removing magnetic energy. Viscosity takes over the role of resistivity, diminishing the effect of lowering the resistivity in simulation A4s.

Although not obvious in the spectra, this effect can be seen by plotting the viscous and resistive dissipation as in figure 8. The aliasing scale is reduced by a factor of 2 in a 256^3 simulation, where it then does not trigger viscous dissipation.

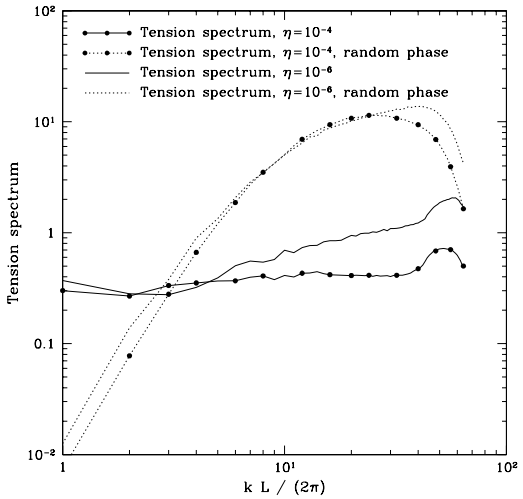

Figure 7: We plot the spectrum of the tension term, $\mathbf{b} \cdot \nabla \mathbf{b}$, to show the effect of lowering the resistivity enough so that aliasing destroys folding structure and enhances tension. The simulations are A4 and A4w, which both have $\nu = 10^{-3}$. A4 has a resistivity of 10^{-4}, and A4w has a resistivity of 10^{-6}. The random phase spectra are obtained by the random phase transformation defined in section C

5.8. Dissipative power

We compare the spectral distribution of energy and dissipation for the saturated state by plotting each quantity logarithmically distributed in k. For the kinetic and magnetic spectra, we plot $\ln(10)kE(k)$, and for the viscous and resistive power, $2\nu \ln(10)k^3 E_v(k)$ and $2\eta \ln(10)k^3 E_b(k)$.

When plotted on a linear ordinate, these curves have the interpretation that the total quantity is equal to the area under the curve.

In figure 8, it is clear for simulation A4 that the magnetic energy resides small scales, and that the high-k cutoff is due to resistivity. Lowering the resistivity by a factor of 3.3 in simulation A4t does not significantly change the magnetic energy spectrum because viscosity takes the place of resistivity at high k. The interpretation is that in simulation A4t, the resistivity is sufficiently low so that aliasing contributes to magnetic energy loss. This destroys magnetic fieldline folding at high k, increases the tension (figure 7), and leads to more viscous dissipation. A proper study of the effect of lowering the resistivity requires that we simultaneously increase the resolution.

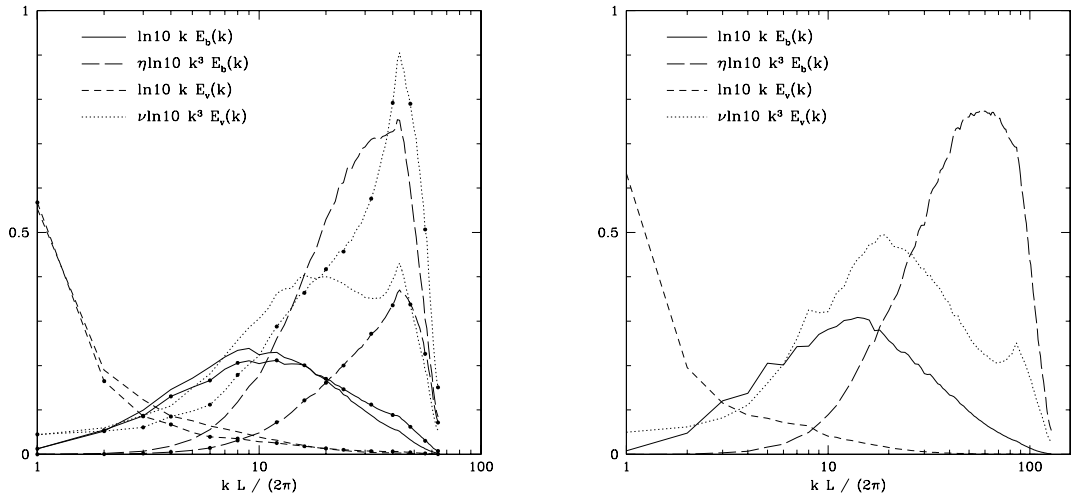

Figure 8. Left: We plot the energy and dissipation per logarithmic k for the velocity and magnetic fields. Lines without dots denote simulation A4, with $\nu = 10^{-3}$ and $\eta = 10^{-4}$. Lines with dots denote simulation A4t, which has the same viscosity and has $\eta = 3 \cdot 10^{-5}$. Right: The energy and dissipation per logarithmic k for the 256^3 simulation B4, which has $\nu = 10^{-3}$ and $\eta = 4 \cdot 10^{-5}$. The magnetic spectrum of simulation B4 farther toward the right in k than for simulation A4.

5.9. Shear and magnetic alignment

The symmetric shear matrix $S = (\partial_i v_j + \partial_j v_i)/2$ can be diagonalized to yield the shear eigenvalues $\{\lambda_+, \lambda_f, \lambda_-\}$ and eigenvectors $\{s_+, s_0, s_-\}$, where we list the eigenvalues from largest to smallest. Incompressibility ensures that $\lambda_+ + \lambda_f + \lambda_- = 0$. The magnetic energy growth is $G = .5 < \partial_t b^2 > = < b_i b_j S_{ij} >$. With the magnetic field projected into the local shear eigenvector frame, this is $G = < b_+^2 \lambda_+ + b_0^2 \lambda_f + b_-^2 \lambda_- >$.

In a nonmagnetized fluid, let a passive scalar c have a diffusivity ζ which is substantially less than ν. ν/ζ is known as the Schmidt number. In the range between λ_ν and λ_ζ, where λ_ζ is the passive scalar diffusion scale, the passive scalar cascade rate is $\epsilon_c \sim c^2/(\lambda_\nu/v_\nu)$, leading to a steady-state cascade index of $E_c(k) \sim k^{-1}$.

Consider two extremes for the orientation of **b** in the shear eigenvector frame. First, if **b** lies principally along s_0, fieldlines are neither being stretched nor compressed, only interchanged, and therefore they cascade without amplification. A profile of **b** in a plane perpendicular to s_0 has an appearance similar to a passive scalar. In this extreme alignment, the power spectrum is $E_b(k) \sim k^{-1}$.

The other extreme is for the fieldlines to be aligned with s_+, so that they are amplified as they cascade. If each reduction in scale is accompanied by a self-similar amplification of energy, the resulting power spectrum index is $E_b(k) \sim k^0$. The geometry of fieldlines in the saturated state must be bracketed by these extremes, therefore the subviscous magnetic spectrum will have an index between -1 and 0. This is observed in figure 3, where the index is closer to -1. The alignment of **b** in the eigenvector frame is found to be preferentially along s_0, which also suggests an index closer to -1.

We measure the saturated-state alignment of **b** in the local shear frame by evaluating $G_2 =< (b_i b_j S_{ij})^2 >$, which is the variance of the magnetic alignment. In the time-averaged saturated state, $G = 0$, and so the mean is zero. We compare this to the result obtained after random-phasing **b** (but not **v**). For a structured field, G_2 has one half the value as for a random-phased field. This establishes that in the local shear frame, **b** preferentially aligns with s_0.

5.10. Forcing scale

Simulation K4 is forced at $3 \leq s \leq 4$, unlike the other simulations which are forced at $1 \leq s \leq 2$. Its purpose is to determine if magnetic energy can occupy modes larger than the forcing scale. The result from figure 9 is that they do not. The initial conditions are taken from the saturated state of simulation A4 at t=19. The viscosity and resistivity are the same as for simulation A4.

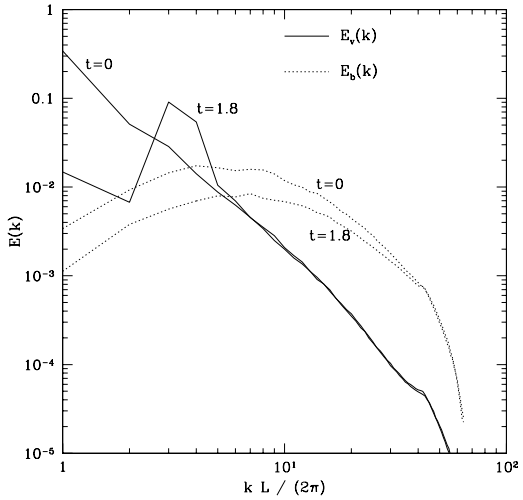

Figure 9: In simulation K4, magnetic energy does not occupy to a significant degree the wavenum-

bers smaller than the forcing wavenumbers at $s = 3, 4$.

5.11. Turbulent diffusivity

For $P_r < 1$, sub-resistive velocities hinder magnetic growth. We establish this with two simulations having the same λ_η and different λ_ν (figure 10). The first (S1) has $\lambda_\nu = \lambda_\eta$, and the second (S2) has $\lambda_\nu \sim 0.4\lambda_\eta$, or $P_r = 0.4$. The second has sub-resistive kinetic energy while the first does not. The resolution of S2 is sufficient to fully capture the dynamics. The magnetic energy in simulation S1 grows more quickly than that for simulation S2. The interpretation is that the sub-resistive eddies act as a turbulent diffusivity on the magnetic field. We will see elsewhere that turbulent diffusivity does not apply for $Pr \geq 1$.

In figure 11, we observe that the magnetic field decays for Prandtl numbers 0.2 and 0.1. However, it is possible that for a simulation with these Prandtl numbers, and a larger grid, that the field might grow instead.

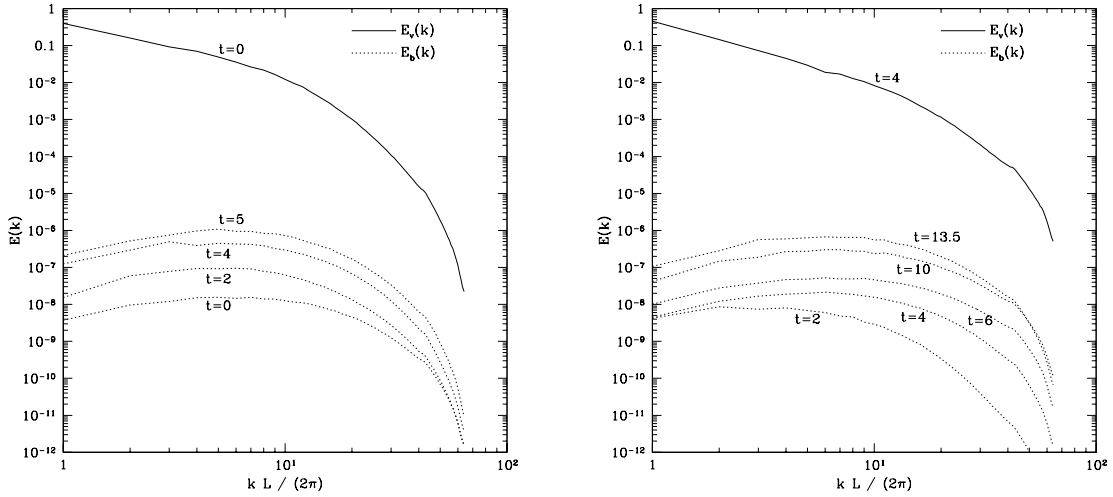

Figure 10. Left: simulation S1, $\nu = 10^{-3}$, $\eta = 10^{-3}$, $Pr = 1$. *The magnetic field grows robustly. Right: simulation S2,* $\nu = 4 \cdot 10^{-4}$, $\eta = 10^{-3}$, $Pr = 0.4$. *The magnetic field grows slowly.*

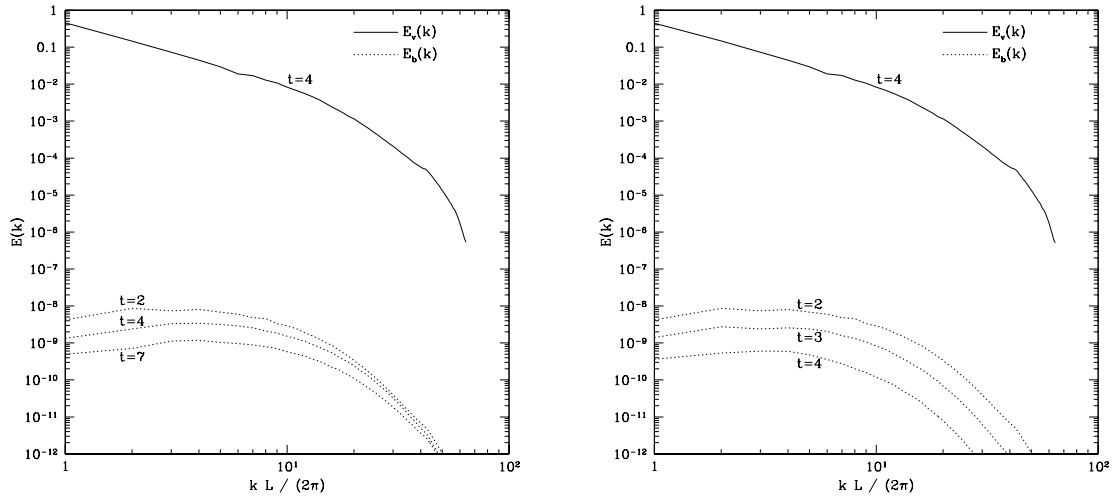

Figure 11. Left: simulation S3, $\nu = 4 \cdot 10^{-4}$, $\eta = 2 \cdot 10^{-3}$, $Pr = 0.2$. Right: simulation S4, $\nu = 4 \cdot 10^{-4}$, $\eta = 4 \cdot 10^{-3}$, $P_r = 0.1$. In each of these simulations, the magnetic field decays.

5.12. Pitfalls

Subtle dangers threaten the validity of turbulent dynamo simulations.

For saturated dynamics, magnetic unwinding causes kinetic motions and viscous dissipation at scales below λ_ν (section Z). Therefore, the use of a hyperviscous operator in the Navier-Stokes equation of the form $\nu_n \nabla^{2n} v$, where $n > 1$, is not valid. If used, it would anomalously destroy small-scale magnetic fields, giving the false impression that the saturated magnetic spectrum does not extend beyond the viscous wavenumber.

In hydrodynamic turbulence, inertial range dynamics are insensitive to whether energy is removed at the inner scale by physical diffusivity or by dealiasing. In MHD turbulence, dealiasing destroys folded fieldline structure, increasing the unwinding and viscous dissipation by a factor of $(\lambda_\parallel/\lambda_\perp)^2$, which can be as large as 200 in our simulations. Therefore, the resistivity must be large enough to prevent magnetic energy from reaching the aliasing scale.

The standard $\alpha - \Omega$ helical dynamo theory assumes that locally, the uniform magnetic field component outweighs the fluctuating component. It is of interest to know if the turbulent dynamo yields a magnetic configuration in accord with this assumption. We therefore emphasize zero helicity and high Prandtl number in our simulations. The astrophysical context has an inertial range of ~ 4 decades and a Prandtl number of $\sim 10^{15}$.

The magnetic field backreacts on the turbulence as it increases in energy after the linear regime, slowing down the shear timescale and increasing the resistive scale according to $t_s \sim \lambda_\eta^2/\eta$. Although the magnetic scale increases, this should not be interpreted as the formation of a large-scale field, as the field is still at the resistive scale. Large resolution and Prandtl number are required to yield

a saturated state where the magnetic energy scale is well separated from the kinetic energy scale.

The $\alpha - \Omega$ helical dynamo theory invokes a concept of turbulent diffusivity acting on the magnetic field. In this picture, turbulence with RMS velocity v at scale λ acts diffusively on the magnetic field with an equivalent viscosity of $v\lambda$. This is at odds with our results, which suggest instead that the magnetic field is cascaded non-diffusively, and only by velocities which have more energy than the magnetic field.

6. Braginskii viscosity

Simulations with Braginskii viscosity are qualitatively similar those with Laplacian viscosity. In figure 12, we see that the field grows quickly in the linear regime, and then reaches a saturated state that is essentially the same as that for the Laplacian viscosity simulations. The difference in the dynamics is that the Braginskii viscosity does not oppose fieldline unwinding, and so the Alfven scaling would apply for the unwinding time. We speculate that topological constraints inhibit the unwinding of small-scale magnetic fields. This is similar to our interpretation in section 5.3 for why a large energy, large-scale magnetic field ultimately evolves to a small-scale field.

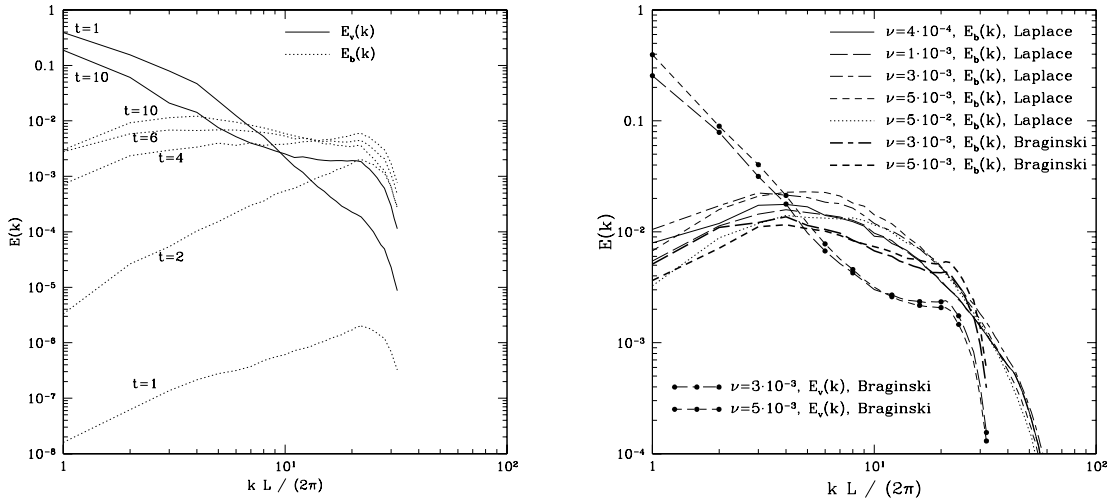

Figure 12. Left: The evolution from the linear to the saturated state for the Braginsky viscosity simulation T3, with $\nu = 3 \cdot 10^{-3}$ and $\eta = 10^{-4}$. Right: The saturated magnetic spectra for two Braginskii viscosity simulations (T2 and T3), shown together with the Laplacian viscosity simulations from figure 3. The resistivity is 10^{-4} in each. The magnetic spectra are nearly the same for each type of viscosity.

7. Acknowledgements

We wish to thank James McWilliams, Alex Schekochihin, Benjamin Chandran, Eric Blackman, Ellen Zweibel, Yoram Lithwick, and Axel Brandenburg for helpful discussions. We benefitted from

the supercomputers at the Caltech Center for Advanced Computing Resources (10000 CPU hours) and at the National Center for Supercomputing Applications at UIUC (10000 CPU hours), and from their very helpful staff.

A. Index of simulations

Table 7: Index of simulations

ID	Grid	ν	η	Pr	Notes
A0	128^3	$5 \cdot 10^{-2}$	0	-	
A1	128^3	$5 \cdot 10^{-2}$	$2 \cdot 10^{-5}$	2500	
A2	128^3	$5 \cdot 10^{-3}$	$1 \cdot 10^{-4}$	50	
A3	128^3	$3 \cdot 10^{-3}$	$1 \cdot 10^{-4}$	30	
A4	128^3	$1 \cdot 10^{-3}$	$1 \cdot 10^{-4}$	10	
A5	128^3	$4 \cdot 10^{-4}$	$4 \cdot 10^{-4}$	1	
B1	256^3	$5 \cdot 10^{-2}$	$1 \cdot 10^{-5}$	2500	
B2	256^3	$5 \cdot 10^{-3}$	$4 \cdot 10^{-5}$	125	
B3	256^3	$3 \cdot 10^{-3}$	$4 \cdot 10^{-5}$	75	
B4	256^3	$1 \cdot 10^{-3}$	$4 \cdot 10^{-5}$	25	
B5	256^3	$4 \cdot 10^{-4}$	$1 \cdot 10^{-4}$	4	
B6	256^3	$1 \cdot 10^{-4}$	$1 \cdot 10^{-4}$	1	
L3	128^3	$3 \cdot 10^{-3}$	$1 \cdot 10^{-4}$	1	Init $\mathbf{b}$ at $k = 4$ with large energy.
L4	128^3	$1 \cdot 10^{-4}$	$1 \cdot 10^{-4}$	1	Init $\mathbf{b}$ at $k = 1$ with large energy.
T2	64^3	$5 \cdot 10^{-3}$	$1 \cdot 10^{-4}$	50	Braginskii viscosity
T3	64^3	$3 \cdot 10^{-3}$	$1 \cdot 10^{-4}$	30	Braginskii viscosity
T3b	64^3	$3 \cdot 10^{-3}$	$4 \cdot 10^{-4}$	7.5	Braginskii viscosity
U4	128^3	$1 \cdot 10^{-3}*$	$1 \cdot 10^{-5}$	100	Erase $\mathbf{v}$ from A4 and continue.
U4r	128^3	$1 \cdot 10^{-3}*$	$1 \cdot 10^{-5}$	100	Like U4, & with random-phased $\mathbf{b}$
K4	128^3	$1 \cdot 10^{-3}$	$1 \cdot 10^{-4}$	100	Force at s=3 & 4.
A4w	128^3	$1 \cdot 10^{-3}$	$1 \cdot 10^{-6}$	1000	Start from weak field
A5w	128^3	$4 \cdot 10^{-4}$	$1 \cdot 10^{-6}$	1000	Start from weak field
A4s	128^3	$1 \cdot 10^{-3}$	$1 \cdot 10^{-6}$	1000	Start from saturated state of A4
A5s	128^3	$4 \cdot 10^{-4}$	$1 \cdot 10^{-6}$	1000	Start from saturated state of A5
S1	128^3	$1 \cdot 10^{-3}$	$1 \cdot 10^{-3}$	1	
S2	128^3	$4 \cdot 10^{-4}$	$1 \cdot 10^{-3}$	0.4	
S3	128^3	$4 \cdot 10^{-4}$	$2 \cdot 10^{-3}$	0.2	
S4	128^3	$4 \cdot 10^{-4}$	$4 \cdot 10^{-3}$	0.1	

The following properties are common to all simulations: The box size is (1,1,1), and the kinetic energy is forced with a power of unity. Forcing occurs within a sphere of radius 2 in Fourier lattice space, except for simulation K4, which is forced at a radius of 3 and 4.

B. Code

We evolve the incompressible MHD equations in Fourier space where they take the form (Lesieur 1990)

$$\partial_t \tilde{v}_\alpha = -ik_\gamma \left(\delta_{\alpha\beta} - \tfrac{k_\alpha k_\beta}{k^2}\right)\left(\widetilde{v_\beta v}_\gamma - \widetilde{b_\beta b}_\gamma\right) - \nu k^{2n}\tilde{v}_\alpha \quad , \tag{B1}$$

$$\partial_t \tilde{b}_\alpha = -ik_\beta(\widetilde{v_\beta b}_\alpha - \widetilde{b_\beta v}_\alpha) - \eta k^{2n}\tilde{b}_\alpha, \tag{B2}$$

$$k_\alpha \tilde{v}_\alpha = 0, \qquad k_\alpha \tilde{b}_\alpha = 0, \tag{B3}$$

$$\partial_t \tilde{c} = -ik_\beta \widetilde{v_\beta c} - \nu_c k^{2n}\tilde{c}. \tag{B4}$$

Equations B1, B2, and B4 constitute a system of ordinary differential equations with time as the dependent variable and the Fourier coefficients $\{\tilde{v}_\alpha, \tilde{b}_\alpha, \tilde{c}\}$ as the independent variables. We employ a modified version of the second order Runge-Kutta algorithm (RK2) to advance the variables in time.

We make one departure from RK2 and treat diffusive terms with an integrating factor. Consider an equation of the form

$$\partial_t \tilde{q}(k) = A - \nu_n k^{2n}\tilde{q}(k), \tag{B5}$$

where A comprises the non-diffusive terms. Its solution, with A constant throughout the interval Δt, is

$$\tilde{q}(\Delta t) = \left[\tilde{q}(0) + \frac{A}{\nu_n k^{2n}}(e^{\nu_n k^{2n}\Delta t} - 1)\right] e^{-\nu_n k^{2n}\Delta t} \tag{B6}$$

We use this expression in place of E1 in each stage of RK2. To lowest order in $\nu_n k^{2n}\Delta t$, equation B6 reduces to E1. However, it has the advantage that it yields stable solutions to equation B5 with constant A for arbitrary values of $\nu_n k^{2n}\Delta t$ whereas E1 yields unstable solutions for $\nu_n k^{2n}\Delta t > 2$

We employ standard dealiasing according to the 2/3 rule (Canuto 1988) except with the Braginskii and ambipolar terms, which require special treatment (section B.1).

The code, written by Maron, is exhaustively discussed in Maron & Goldreich 2000.

Define the one-dimensional kinetic and magnetic energy spectra as

$$E_v = \int E_v(k)dk \qquad E_b = \int E_b(k)dk \tag{B7}$$

B.1. The Braginskii term

Bilinear terms in the MHD equations are calculated by transforming the individual fields to real space, carrying out the appropriate multiplications there, and then transforming the products back to Fourier space. This requires $N_1 N_2 N_3$ operations using the Fast Fourier Transform (FFT)

algorithm; $(N_1 N_2 N_3)^2$ operations would be needed to carry out the equivalent convolution in Fourier space.

This economy comes at the price of either a 1/3 reduction in resolution or an aliasing error. To appreciate this, consider the 1D product

$$\begin{aligned} \widetilde{pq}(s) &= \tfrac{1}{N}\sum_l \left[\sum_{s'} \tilde{p}(s') e^{-2\pi i s' l/N} \sum_{s''} \tilde{q}(s'') e^{-2\pi i s'' l/N}\right] e^{2\pi i s l/N} \\ &= \tfrac{1}{N}\sum_{s'}\sum_{s''} \tilde{p}(ß') \tilde{q}(s'') e^{2\pi i (s'+s'') l/N} \delta_{s,s'+s''+mN}, \end{aligned} \tag{B8}$$

where m is any integer. The $m = 0$ terms comprise the convolution, and the remainder the aliasing error. To avoid the aliasing error, we set all Fourier components with $|s| > N/3$ to zero both before we compute the real space fields and again after we return the bilinear terms to Fourier space. Truncation ensures that Fourier components of bilinear terms with $m \neq 0$ vanish. Its cost is the reduction of the effective spatial resolution from N to $2N/3$.

The Braginskii term contains a product of 5 fields inside the gradient, plus two divisions by b^2. When M terms are multiplied, dealiasing should be applied for $|s| < N/(M+1)$, however the division will introduce aliased terms regardless of the location of the truncation. The appropriate procedure then becomes a matter of engineering. The rule we apply to decide if the computation is sufficiently accurate is that it should agree with the equivalent computation performed on an infinitely large grid. We find that a truncation of $|s| < N/3$ is inadequate for the Braginskii term, and that a truncation of $|s| < N/6$ is more than adequate (figure 13).

To test the properties of the dealiasing truncation, we evaluate the Braginskii term for two grid sizes, with the larger grid regarded as the "correct" result and the smaller grid the "test" result. We apply the same dealiasing truncation to both grids before and after the computation before comparing. We then varied the location of the dealiasing truncation for different pairs of grids. In table 8, pairs A-B, C-D, and E-F all share the same truncation. The input fields are taken from simulation Z65 at $t = 4$. The magnetic field is dominated by small scale structure and presents a worst case scenario for alias error. In figure 13, we selected the Braginskii term's $\hat{x}$ component and plotted it as a function of x at fixed y and z for each grid pair. Test grid F, with a truncation at $N/3$, shows poor agreement with the larger grid E.

We conclude that the MHD terms should be dealiased at $N/3$ and the Braginskii term at $N/6$. We implement this by computing the MHD terms on a size N^3 and the Braginskii term on a $(2N)^3$ grid. The Braginskii result is then returned to a N^3 grid and added to the MHD result. Aside from economizing resolution, this configuration also economizes timestep. The timestep will be set by the N^3 grid, which is twice as large as the timestep that would be necessary for the $(2N)^3$ grid.

Table 8: Braginskii viscosity test simulations.

ID	Grid	Truncation	ID	Grid	Truncation
A	64^3	$\|s\| < 32/6$	B	32^3	$\|s\| < 32/6$
C	64^3	$\|s\| < 32/4$	D	32^3	$\|s\| < 32/4$
E	64^3	$\|s\| < 32/3$	F	32^3	$\|s\| < 32/3$

The ambipolar term is computed by first obtaining the magnetic force and then putting it in the place of v in the induction equation. This requres that we dealias the magnetic force before computing the rest of the induction term.

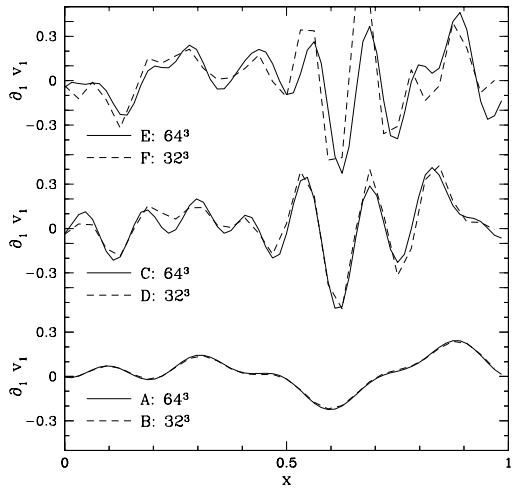

Fig 13: Alias error in the Braginskii term. Curve B is the Braginskii term computed with a dealiasing truncation at N/6, which agrees will with the equivalent simulation on a larger grid. The dealiasing truncation in curves D and F is at N/4 and N/3 respectively. The N/3 truncation leads to poor agreement.

C. Random phase transformation

Structure in the dynamical fields can be studied through comparison with their random-phase realizations. The random phase transformation is designed to remove the coherent structure while preserving the power spectrum. The transformation is accomplished by giving each Fourier mode vector $\mathbf{v}(k)$ and $\mathbf{b}(k)$ a new random orientation while preserving the magnitude, subject to the constraint of divergencelessness.

REFERENCES

[1]Armstrong, J. W., Rickett, B. J., & Spangler, S. R. 1995, ApJ, 443, 209

[2]Batchelor, G. K. 1950, Proc. Roy. Soc. Lon. A201, 405.

[3]Beck, R., Brandenburg, A., Moss, D., Shukurov, A. and Sokoloff, D. 1996, Annu. Rev. Astron. Astrophys. **34** 155.

[4]Biermann, L., Z. Naturforsch 5a, 65(1950)

[5]Braginskii, S. I. 1965, Rev. Plasma Phys. 1, 205.

[6]Chandran, B., Cowley, S., 1998, PRL V80, no. 14.

[7]Chandran, B.D.G., 2000, PRL, in press

[8]Chertkov, M., Falkovich, G., Kolokolov, I. & Lebedev, V. 1999, Phys. Rev. Lett. 83, 4065.

[Glatzmaier and Roberts 95]Glatzmaier, G.A. and Roberts, P.H., 1995, Nature, 377, 203.

[9]Field, G.B., Blackman, E.G. & Chou, H. 1999, Ap. J. 513, 638.

[10]Gnedin N., Ferrara, A. and Zweibel, E.G. 2000, Ap. J. 539, 505.

[11]Goldreich, P. & Sridhar, S. 1995, ApJ, 438, 763

[12]Goldreich P. & Sridhar, S. 1997, ApJ, 485, 680

[13]Gruzinov, A., Cowley, S., Sudan, R. 1996, Phys. Rev. Lett. 77, 43, 42.

[14]Heiles, C., Presented at the 4th Tetons summer conference: "Galactic structure, stars, and the interestellar medium."

[15]Kazantsev, A. P. 1968, Sov. Phys. JETP, 26, 1031.

[16]Kinney, R. M., Chandran, B. D. G., Cowley, S. C., McWilliams, J. C., American Astronomical Society Meeting, 192, 66.18, 1998

[17]Kinney, R. M., Chandran, B., Cowley, S., McWilliams, J. C., 2000, ApJ, 545, 907.

[18]Kraichnan, R. & Nagarajan, S. 1967, Phys. Fluids, 10, 859,

[19]Kronberg, P. 1994, Rep. Prog. Phys 59 325.

[20]Kulsrud, R., & Anderson, S., 1992, ApJ, 396, 606

[21]Kulsrud, R., Cen, R., Ostriker, J. P., & Ryu D., 1997, ApJ, 480, 481

[22]Kulsrud, R., & Pearce, W., 1969, ApJ, 156, 445

[23]Kulsrud, R.M., 1999, Annu. Rev. Astron. Astrophys.

[24]Lesieur, M. 1990, Turbulence In Fluids (Dordrecht:Kluwer)

[25]Maron, J., Goldreich, P., 2001, ApJ, 554, 1175

[26]Maron, J., Blackman, E., 2001, PRL, submitted.

[27]Moffatt, H. K., 1978, Magnetic field generation in Electrically Conducting Fluids, Cambridge University Press: Cambridge

[28]Parker, E.N. 1979, Cosmical Magnetic Fields (Oxford:Oxford Univ. Press)

[29]Rosenbluth, Kaufman, Phys Rev 109, 1, 1958

[30]Ruzmaikin, A. A., Shukurov, A. M., & Sokoloff, D. D., Magnetic Fields of Galaxies (Dordrecht: Kluwer)

[33]Schekochihin, A. A., Boldyrev, S. A., Kulsrud, R. M. 2001, astro-ph/0103333, submitted to ApJ.

[32]Schekochihin, A., Ph.D. Thesis, Princeton University, 2000.

[33]Schekochihin, A., Cowley, S., Maron, J., Malyshkin, L., PRE, accepted.

[34]Spangler, S. R. & Cordes, J., ApJ, 505, 766, 1998

[35]Spitzer, "Physical Processes in the Interstellar Medium", 1978

[36]Sridhar S. & Goldreich, P. 1994, ApJ, 432, 612

[37]Taylor, G. B., Allen, S. W., Fabian, A. C., 1999, Proceedings of the workshop: "Diffuse thermal and relativistic plasma in galaxy clusters", 77-81.

[38]Vainshtein, S. I., & Kichatinov, L. L. 1986, J. Fluid Mech., 168, 73

[39]Vallee, J. P., Fundamental Cosmic Physics, 1998, 19, 319-422.

[40]Zweibel, E.G. and Heiles, C. 1997, Nature, 131.